THE JOURNAL OF PHYSICAL CHEMISTRY Letters

Letter

pubs.acs.org/JPCL

Rate-Dependent Nucleation and Growth of NaO_2 in $Na-O_2$ Batteries

Nagore Ortiz-Vitoriano,*[,†,‡,⊥,#] Thomas P. Batcho,[‡,§,#] David G. Kwabi,[‡,∥,#] Binghong Han,[‡,§] Nir Pour,[†,‡] Koffi Pierre Claver Yao,[‡,∥] Carl V. Thompson,*[,§] and Yang Shao-Horn*[,†,‡,§,∥]

[†]Research Laboratory of Electronics, [‡]Electrochemical Energy Laboratory, [§]Department of Materials Science & Engineering, and [∥]Department of Mechanical Engineering, Massachusetts Institute of Technology, 77 Massachusetts Avenue, Cambridge, Massachusetts 02139, United States

[⊥]CIC EnergiGUNE, Parque Tecnológico de Álava, Albert Einstein 48 - ED, CIC 01510 Miñano, Álava, Spain

Supporting Information

ABSTRACT: Understanding the oxygen reduction reaction kinetics in the presence of Na ions and the formation mechanism of discharge product(s) is key to enhancing $Na-O_2$ battery performance. Here we show NaO_2 as the only discharge product from $Na-O_2$ cells with carbon nanotubes in 1,2-dimethoxyethane from X-ray diffraction and Raman spectroscopy. Sodium peroxide dihydrate was not detected in the discharged electrode with up to 6000 ppm of H_2O added to the electrolyte, but it was detected with ambient air exposure. In addition, we show that the sizes and distributions of NaO_2 can be highly dependent on the discharge rate, and we discuss the formation mechanisms responsible for this rate dependence. Micron-sized (~500 nm) and nanometer-scale (~50 nm) cubes were found on the top and bottom of a carbon nanotube (CNT) carpet electrode and along CNT sidewalls at 10 mA/g, while only micron-scale cubes (~2 μm) were found on the top and bottom of the CNT carpet at 1000 mA/g, respectively.

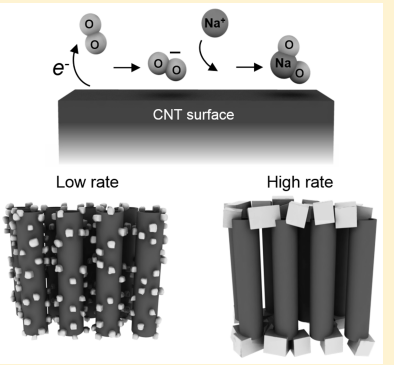

Rechargeable metal-air (oxygen) batteries are receiving intense interest as possible alternatives to lithium-ion batteries, in particular due to their potential to provide higher gravimetric energies.[1−5] While much attention has been focused on aprotic $Li-O_2$ batteries since their introduction in 1996 by Abraham et al.,[6] substantial challenges must be addressed before widespread commercial exploitation is possible. These include the instability of aprotic electrolytes[7−9] and oxygen electrodes,[10,11] which contribute to low round-trip efficiency, poor rate capability, and poor cycle life. Recently, a metal-air battery in which lithium has been replaced by sodium has received increasing attention.[12] Although $Na-O_2$ batteries present lower gravimetric energies on a cell basis (1605 or 1108 Wh/kg based on Na_2O_2 or NaO_2 discharge products, respectively)[12] than $Li-O_2$ batteries (3505 $Wh/kg_{Li_2O_2}$),[2] much lower charge overpotentials (~100 mV) than those in typical $Li-O_2$ batteries (~1000 mV) have been reported[13,14] based on reversible sodium superoxide (NaO_2) formation ($Na + O_2 \leftrightarrow NaO_2$, $E^0 = 2.27$ V). Unlike $Li-O_2$ batteries, for which Li_2O_2 is the only discharge product, NaO_2,[12−15] sodium peroxide (Na_2O_2),[16,17] and sodium peroxide dihydrate ($Na_2O_2{\cdot}2H_2O$),[18,19] or a mixture,[19−21] have been identified in $Na-O_2$ batteries in ether-based electrolytes using a range of carbon electrode types. These products have been shown to have different morphologies: NaO_2 in micron-scale cubic shapes[12,14] and nanorods,[22] Na_2O_2 in polycrystalline particles,[16] and $Na_2O_2{\cdot}2H_2O$ as rod-shaped particles or thin films.[20] Unfortunately, the factors responsible for dissimilar discharge product chemistry and morphologies are still unclear, and no correlation has been found between the type of air electrode or electrolyte and the discharge product formed. Because the discharge product crystal structure, morphology (e.g., shape and thickness), and distribution are important parameters that influence the voltage profile on discharge and charge, the rate capability, the discharge capacity, and the reversibility in metal-air batteries,[23] it is critical to gain insights into the oxygen reduction kinetics in the presence of Na ions and the nucleation and growth mechanisms of discharge products.

In this study, we investigate discharged $Na-O_2$ cells with carbon nanotube (CNT) carpet cathodes to understand the effect of discharge kinetics on the formation of the discharge product. We analyzed the chemical composition of the discharge product using X-ray diffraction (XRD) and Raman spectroscopy and found that it consisted solely of NaO_2. The formation of $Na_2O_2{\cdot}H_2O$ was not readily detected with the addition of water to the solvent (<6000 ppm); however, the evolution of $Na_2O_2{\cdot}2H_2O$ was detected when we intentionally exposed the sample to the ambient environment. We also observed rate-dependent effects on the size and distribution of the discharge product. At high rates, micron-sized cubes were formed on the top and bottom interfaces between the CNT carpet and electrolyte, while at low rates, the entire thickness of the CNT carpet was more homogeneously covered with faceted nanoparticles. We show that this difference is consistent with

Received: May 4, 2015
Accepted: June 18, 2015

DOI: 10.1021/acs.jpclett.5b00919
J. Phys. Chem. Lett. 2015, 6, 2636−2643

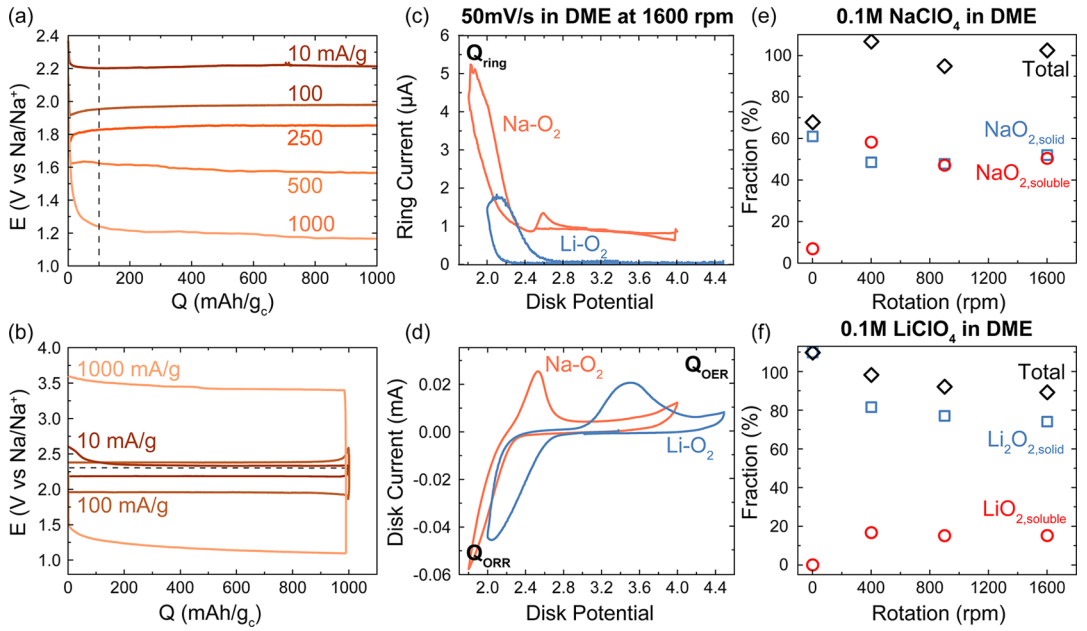

Figure 1. (a) Voltage versus capacity of CNT electrodes discharged galvanostatically between 10 and 1000 mA g_C^{-1} in 0.1 M $NaClO_4$ in DME. (b) Discharge and charge voltage profiles of Na−O_2 cells to a fixed capacity (1000 mAh g_c^{-1}). Dotted line: E^0 (NaO_2) = 2.27 V. RRDE measurements of the ORR/OER in 0.1 M $NaClO_4$ and $LiClO_4$ in DME at 1600 rpm showing (c) current response on the ring, which is held potentiostatically at 3.0 V versus Na^+/Na or 3.5 V versus Li^+/Li, (d) CVs on the disk at 50 mV/s between 1.8 and 4.0 V versus Na^+/Na and 2.0−4.5 versus Li^+/Li, and estimated soluble and insoluble fractions of the total ORR charge as a function of rotation rate in (e) 0.1 M $NaClO_4$ and (f) 0.1 M $LiClO_4$ in DME.

fast NaO_2 nucleation from solvated growth precursors at high rates, while at lower rates, diffusion of those precursors facilitates uniform growth of smaller nanoparticles.

We first examine the oxygen reduction reaction (ORR) kinetics of NaO_2 formation on CNT electrodes upon galvanostatic discharge. The CNT electrodes were carpets (~1 cm × ~1 cm × ~500 μm) of freestanding vertically aligned nanotubes with no binder. Figure 1a,b shows the voltage profiles at discharge rates of 10, 100, 250, 500, and 1000 mA g_c^{-1} to a fixed capacity of 1000 mAh g_c^{-1} and the discharge and charge curves of electrodes cycled at different rates to a fixed capacity (1000 mAh g_c^{-1}). A single flat discharge plateau is observed at all rates. At low current densities, a voltage plateau of 2.21 V corresponding to an overpotential of 60 mV is observed, similar to that obtained by Hartmann et al. (~100 mV),[12] while at high current densities this overpotential increases. This trend is consistent with data extracted from analogous Na−O_2 discharge experiments on different carbon surfaces, although exact values differ from those of the CNTs reported herein, as shown in the Tafel plot of overpotential versus discharge current normalized to true cathode surface area in Figure S1 in the Supporting Information (SI). The charging process (Figure 1b), at low and medium current densities of 10 and 100 mA g_c^{-1}, occurs at voltage plateaus of 2.33 and 2.38 V, respectively, which is close to the potential for the decomposition of NaO_2 to form Na^+ and oxygen (E^0 = 2.27 V) and in good agreement with that reported by Hartmann et al.[12] (2.3 to 2.4 V). These low-charge overpotentials differ from the larger overpotentials observed in Li−O_2 batteries,[23,24] and might indicate a different charging reaction mechanism in these two systems. If the discharge overpotential between 0.01 and 0.1 μA cm_c^{-2} (i.e., 100−500 mA g_c^{-1}) is taken to have a linear dependence on the log of discharge current (Figure S2 in the SI), this is consistent with a kinetically controlled ORR process.[23,25] The corresponding Tafel slope (~240 mV per decade) is in good agreement with that reported for Li−O_2 cells using CNT electrodes (290 mV per decade, Figure S1 in the SI).[23] At low (<0.01 μA cm_c^{-2} or 10 mA g_c^{-1}) and high current densities (>0.1 μA cm_c^{-2} or 1000 mA g_c^{-1}), however, the overpotential deviates from linear, Butler−Volmer-type behavior and decreases rapidly with increasing discharge current. It is interesting to note that Viswanathan et al.[26] report similar nonconstant Tafel behavior on glassy carbon electrodes in Li−O_2 cells, where linear behavior was observed at discharge currents <0.1 μA cm_C^{-2}. Recently, Safari et al.[27] developed a kinetic model for ORR in Li−O_2 cells that led them to suggest that the curvature in the Tafel plot originates from a finite kinetic mismatch between reduction of adsorbed oxygen and adsorbed lithium-superoxide. They reported that this curvature is due to the contribution of superoxide disproportionation and irreversible side reactions to the measured electrode potential. A recent study by Bai et al.[28] has, however, shown that the kinetic behavior of carbon-coated $LiFePO_4$ electrodes, which also exhibit a nonconstant Tafel slope, closely matches predictions from Marcus−Hush−Chidsey theory, with the curvature controlled by the reorganization energy of reactant and product species involved in electron transfer. The similarity between Tafel behavior in Li−O_2 and Na−O_2 batteries might therefore indicate a common rate-determining step (i.e., electron transfer to O_2 to form LiO_2 or NaO_2); however, further investigations of Na−O_2 battery kinetic behavior are needed to better understand the deviations at low and high currents.

To probe the influence of soluble reaction intermediates on fundamental kinetic processes involved in Na−O_2 electrochemistry, we performed cyclic voltammetry (CV) measurements of ORR/OER on a smooth glassy carbon disk surface in O_2-saturated 0.1 M $NaClO_4$ in DME using the rotating ring disk electrode (RRDE), with an Au ring used to oxidize soluble ORR products. Ring and disk current response curves in

DOI: 10.1021/acs.jpclett.5b00919
J. Phys. Chem. Lett. 2015, 6, 2636−2643

Figures 1c,d, respectively, show that a greater number of soluble ORR intermediates are produced in Na^+ than in the analogous Li^+ electrolyte during the cathodic sweep when the ORR takes place. This difference was quantified in terms of the fraction of ORR charge (Q_{ORR}) composed of soluble (Q_{ring})/insoluble (Q_{OER}) species as a function of rotation rate in Figure 1e,f and provides a basis for investigating how differences in Li−O_2 versus Na−O_2 discharge product distribution and morphologies can be explained using LiO_2 versus NaO_2 nucleation rates. These implications will be discussed in further detail later. During the anodic sweep, we observe an oxidation peak at 2.6 V versus Na^+/Na on the ring, suggesting the participation of soluble species during NaO_2 decomposition. This is in stark contrast with the Li−O_2 case, where Li_2O_2 decomposition has been hypothesized to occur via solid-state delithiation,[23,25,29] and, accordingly, no such anodic peak is observed. This difference points to the presence of fundamentally different intermediate species during 2- versus 1-electron peroxide/superoxide oxidation processes, and whose precise identities future studies should investigate in greater detail using spectroscopic/structural methods.

Phase-pure NaO_2 (pyrite structure, $Fm\bar{3}m$) was found as the only discharge product, confirmed by XRD and Raman spectroscopy. Figure 2a shows the XRD patterns for the CNT electrodes discharged at 10, 100, and 1000 mA g_c^{-1} to 1000 mAh g_c^{-1}. Both diffraction peak positions and intensities agree well with NaO_2 (JCPDS reference card no. 01-077-0207). The other reflection maxima indicated in the diffractograms are related to the aluminum gastight sample holder. Moreover, Raman spectra support that NaO_2 is the main discharge product due to the presence of an intense peak at 1156 cm^{-1} (Figure 2b), previously reported to be characteristic of this chemistry.[30] It is important to note that carbonate species can be observed by Raman and have been observed upon discharge in alkyl carbonate-based electrolytes.[18] We see no clear evidence of carbonate species, which is in agreement with recent differential electrochemical mass spectrometry (DEMS) analysis of Na−O_2 discharge,[15] and suggests the formation of only trace amounts of carbonate side products upon discharge. The reversibility of the reaction on charge was also confirmed using XRD (Figure 2a), which shows that NaO_2 diffraction peaks completely disappear after charging.

We show, for the first time, that NaO_2 can be converted to $Na_2O_2{\cdot}2H_2O$ upon exposure to ambient atmosphere for short times (Figure 2c,d). While XRD revealed phase-pure NaO_2 for discharged electrodes in the sealed XRD holder after 1 h (Figure 2a), $Na_2O_2{\cdot}2H_2O$ (JCPDS 15-0064) was found to appear after longer scans of 2 and 3 h, which could be attributed to the reactivity of NaO_2 and water in ambient air associated with the leakage of the XRD holder. The fraction of the $Na_2O_2{\cdot}2H_2O$ phase increases after 3 h of exposure, becoming the dominant phase. The formation of $Na_2O_2{\cdot}2H_2O$ upon exposure of NaO_2 to ambient air is supported using Raman spectroscopy (Figure 2d), for which a characteristic peak for $Na_2O_2{\cdot}2H_2O$ appeared in addition to the NaO_2 peak (Figure S3 in the SI). The high reactivity of NaO_2 in air to form $Na_2O_2{\cdot}2H_2O$ may explain the appearance of these two discharge products in Na−O_2 cells[18−20] reported in the literature if the discharge products were exposed to ambient air or considerable amounts of water. In this regard, several cells with electrolyte water content between 10 and 6000 ppm were examined upon galvanostatic discharge to observe the influence of water content on the discharge product (Figure S4 in the SI). Figure S4a shows the voltage profiles for cathodes discharged in electrolytes of various water contents at 100 mA g_c^{-1} to a fixed capacity of 1000 mAh g_c^{-1} or 2000 mAh g_c^{-1} for the cell discharged with 6000 ppm of water. Phase-pure NaO_2 (pyrite structure, $Fm\bar{3}m$) was found as the main discharge product, confirmed by Raman spectroscopy (Figure S4b in the SI) and XRD (Figure S4c) in all cells with up to 6000 ppm of water content in the electrolyte. Although the exact water content in the electrolyte could be influenced by reactivity with the Na negative electrode, increasing water content from 10 to 6000 ppm in the electrolyte led to changes in the NaO_2 morphology (Figure S5 in the SI), while no changes were found in the XRD data of the discharged product. This observation is in agreement with a recent study by Xia et al.[31] reporting Na−O_2 discharge behavior in glyme-based electrolytes with up to 100 000 ppm of H_2O, where only NaO_2 was reported. These results therefore suggest that the conversion of $Na_2O_2{\cdot}2H_2O$ could not result from the reactivity between NaO_2 and H_2O alone, for which ~6400 ppm of water is required for direct conversion of all discharged NaO_2 to $Na_2O_2{\cdot}2H_2O$. (See the SI for details of this calculation.)

The size and distribution of NaO_2 particles are a function of discharge rate. Figure 3a,b shows SEM images of the CNT electrode top surface (the O_2/electrode interface) at 10 and

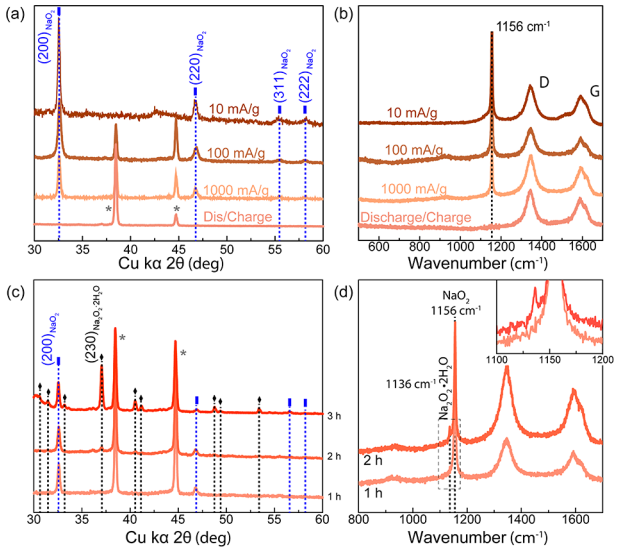

Figure 2. (a) XRD patterns and (b) Raman spectra for the CNT electrodes discharged at 10, 100, and 1000 mA g_c^{-1} to 1000 mAh g_c^{-1}(corresponding discharge profiles shown in Figure 1a) and after being discharged and fully charged at 1000 mA g_c^{-1} to 1000 mAh g_c^{-1} in 0.1 M $NaClO_4$ in DME. D and G bands of the CNTs and the NaO_2 peak at 1156 cm^{-1} are indicated in the Raman spectra. (c) XRD patterns of a CNT electrode discharged at 1000 mA g_c^{-1} to 2000 mAh g_c^{-1} in 0.1 M $NaClO_4$ in DME, showing the conversion to $Na_2O_2{\cdot}2H_2O$ (black dashed lines) from NaO_2 (blue dashed lines) in the XRD holder after 1, 2, and 3 h at ambient. The CNT electrodes were extracted from the Na−O_2 cell immediately after discharge in an argon-filled glovebox and sealed in an airtight XRD sample holder (Anton Paar, Graz, Austria). The first diffractogram (labeled 1 h) was collected immediately after 1 h of cell discharge. Subsequent diffractograms (2 h and 3 h) were collected sequentially, each with a collection time of 1 h. (d) Raman spectra of a CNT electrode discharged at 1000 mA g_c^{-1} to 2000 mAh g_c^{-1} in 0.1 M $NaClO_4$ in DME taken immediately after discharge (labeled 1 h) and after 1 h of exposure to air (labeled 2 h), showing evolution of Na_2O_2 $2H_2O$ (1136 cm^{-1}) from NaO_2 (1156 cm^{-1}).

DOI: 10.1021/acs.jpclett.5b00919
J. Phys. Chem. Lett. 2015, 6, 2636−2643

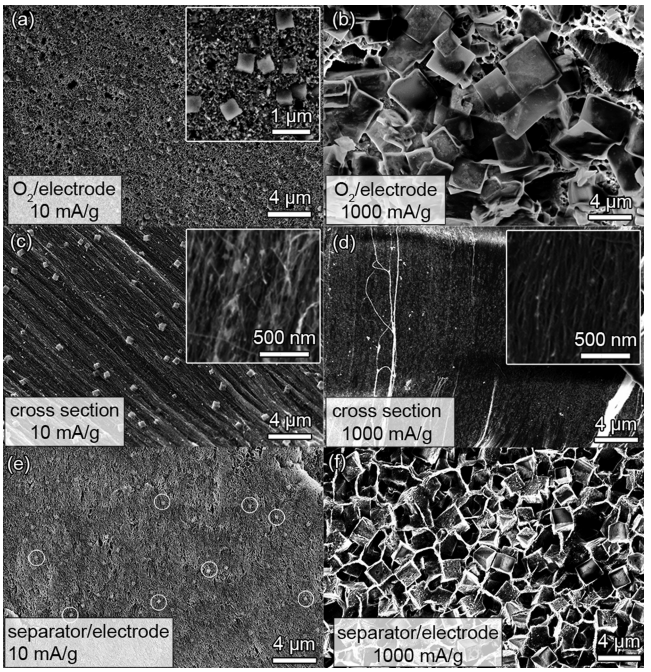

Figure 3. SEM images of galvanostatically discharged CNT electrodes at (a,c,e) 10 mA g_c^{-1} and (b,d,f) 1000 mA g_c^{-1} to 1000 mAh g_c^{-1}, showing the O_2/electrode (a,d) and separator/electrode (c,f) interfaces and cross sections of the CNT carpets (b,e), respectively.

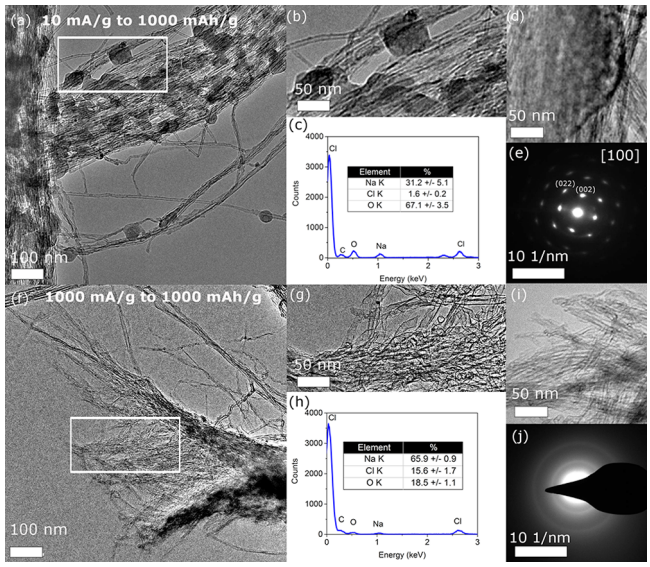

Figure 4. TEM images of galvanostatically discharged CNT electrodes at (a,b,d) 10 mA g_c^{-1} and (f,g,i) 1000 mA g_c^{-1} to 1000 mAh g_c^{-1}. (b,g) Higher magnification images of regions in white boxes in panels a and f. (c,h) Energy-dispersive X-ray spectroscopy (EDS) spectrum from panels a and f. (e,j) Electron diffraction patterns from panels d and j, respectively.

1000 mA g_c^{-1} to 1000 mAh g_c^{-1}, where the top surface was covered with cubes characteristic of NaO_2 crystals. At low discharge rates (i.e., 10 mA g_c^{-1} or 0.01 μA cm_C^{-2}), submicron-scale ~500 nm NaO_2 cubes partially cover the surface (Figure 3a), whereas at high discharge rate (i.e., 1000 mA g_c^{-1} or 0.1 μA cm_C^{-2}) the NaO_2 cubes were considerably bigger (~2−10 μm) and cover the majority of the surface (Figure 3b). Figure 3c,d shows SEM images of interior cross sections of CNT carpets discharged at 10 and 1000 mA g_c^{-1} to 1000 mAh g_c^{-1}. Upon discharge at 10 mA g_c^{-1}, we find sub-micron-scale cubes and small cubes and particles with sizes of ~50 nm (Figure 3c), whereas at 1000 mA g_c^{-1} the cross sections of the CNT carpets are mostly bare (Figure 3d). NaO_2 cubes (~400 nm at 10 mA g_c^{-1} and 1.5 to 2.5 μm at 1000 mA g_c^{-1}) were also found at the separator/electrode interface (Figure 3e,f). Differences in sizes of sub-micron-scale cubes for the oxygen interface and cross-section at 10 mAg_c^{-1} (Figure 3a,c) fell within the variation from region to region, while the sizes of cubes close to the separator interface were consistently smaller than those at the current collector interface (Figure 3e). Analysis of electrodes discharged at different gravimetric rates but the same capacity (Figure S6 in the SI) shows that the density of the nanosized faceted particles decreases with increasing discharge rate.

TEM imaging clearly shows nanometer-scale cubes and particles along CNT sidewalls in electrodes discharged at 10 mA g_c^{-1} (Figure 4a), in contrast with largely bare CNTs at 1000 mA g_c^{-1} (Figure 4f). The nanoparticle sizes remained largely unchanged with increasing discharge capacity (Figure S7 in the SI). Energy-dispersive X-ray spectroscopy (EDS) (Figure 4c and 4h) revealed that after correcting for $NaClO_4$ already in the electrode (Figure S8 in the SI), these nanometer-scale particles like micron-scale cubes (Figure 4c,h) have a 1:2 ratio of Na to O, corresponding to NaO_2 chemistry. Nanometer-scale NaO_2 did not form along CNT sidewalls for electrodes discharged at 1000 mA g_c^{-1}, as evidenced by EDS (Figure 4h), which showed an elemental composition consistent with the $NaClO_4$ salt, and electron diffraction (Figure 4j). The formation of these particles on CNTs was further supported by selected-area electron diffraction (SAED) patterns (Figure 4e and Table S1 in the SI), where all electron diffraction patterns collected could be indexed with the $Fm\bar{3}m$ structure of NaO_2.

The precise growth mechanism responsible for the formation of micron-scale NaO_2 cubes remains a matter of considerable debate.[13,31] NaO_2 cubes shown in Figure 3 are consistent with the theoretical Wulff shape reported by Lee et al.,[32] and the faceted shapes suggest a classical layer-by-layer growth mechanism, which has been proposed in pyrite FeS_2 (pyrite).[33] NaO_2 cubes in this work also appear to display penetration twinning (Figure S9a in the SI), caused by the growth of misoriented crystals with common lattice points, and surface faceting (Figure S9b in the SI), both of which have been observed in FeS_2. A fully analogous growth mechanism for NaO_2 to pyrite growth,[13] where O_2 reduction to O_2^- is followed by stepwise Na^+ addition on the solid NaO_2 surface, is, however, unlikely given that (1) NaO_2 has been widely assumed to be electrically insulating,[34,35] which is supported by recent density functional theory (DFT) calculations,[36,37] thus making direct O_2 reduction on the NaO_2 surface in layer-by-layer fashion difficult to envision and (2) ORR products have significant solubility in DME, which has been previously speculated[13] and measured by RRDE here (Figure 1c,e) and in a recent study by Xia et al.[31] NaO_2 solubility in aprotic electrolytes raises the possibility that NaO_2 cubes can grow via mesoscale self-assembly[31,38] of solvated precursor species and high-order aggregates, similar to other electrically insulating metal oxide crystals[38] such as $BaSO_4$, ZnO, and $CaCO_3$. It is worth noting that similar solution-mediated mechanisms have been proposed for Li_2O_2 growth in Li−O_2 batteries.[39,40] Further investigation of the electronic transport properties of NaO_2 and the effect of different solvents on NaO_2 morphology

DOI: 10.1021/acs.jpclett.5b00919
J. Phys. Chem. Lett. 2015, 6, 2636−2643

is essential to clarify details about this mechanism and is currently underway by the authors.

Large NaO_2 cubes found in regions of the carpet that have easy access to oxygen (O_2/electrode and electrode/separator interfaces) from high-rate discharge can be primarily explained by high NaO_2 formation rates. Indeed, previous studies have reported that the location of NaO_2 cubes in discharged carbon paper-based cathodes is highly dependent on the spatial variation of oxygen concentration in the cathode, such that a much higher concentration of cubes is found in regions/interfaces in direct contact with oxygen, than otherwise.[13,41,42] To investigate the hypothesis that the spatial variation in NaO_2 cube density at 1000 mA g_C^{-1} could reflect a variation in local oxygen concentration across the CNT carpet, we modeled the steady-state distribution of oxygen in the electrolyte-filled pores across the electrode cross section by combining Fick's diffusion law with electrochemical O_2 reduction parameters set by the applied current. (See the calculation in the SI.) The concentration of O_2 in the electrolyte-filled pores from the oxygen-rich interfaces toward the interior of the electrode is shown in Figure S10 in the SI. At low rates (10−100 mA g_c^{-1}), there is a negligible drop in the O_2 concentration across the electrode thickness. This is consistent with the ORR and thus solid NaO_2 formation occurring uniformly throughout the CNT carpet. In contrast, at 1000 mA g_c^{-1}, a ∼60% drop in the O_2 concentration across the electrode is expected. This result is, however, at odds with TEM images of electrodes discharged at 1000 mA g_c^{-1} (Figure 4f), where there is negligible discharge product in the electrode interior. It is additionally inconsistent with what we observe in CNT cathodes discharged at a comparable rate of 1000 mA g_c^{-1} in 0.1 M $LiClO_4$ in DME, where no Li_2O_2 toroids are observed,[23,43] and the discharge product is typically more uniformly distributed (Figure S11 in the SI), although similar steady-state oxygen concentrations would be expected in that electrolyte. Thus, using the steady-state O_2 concentration model, the moderate concentration gradient of molecular oxygen found in the electrolyte at high rates such as 1000 mA/g (SI) is not sufficient to explain the formation of large NaO_2 crystals on the top and bottom of the CNT carpet but not within it.

A more likely hypothesis is one in which the NaO_2 particle size and distribution is dictated by the concentration of reduced O_2^--Na^+ species in the electrolyte and the nucleation and diffusion of $(O_2^-\text{-}Na^+)_n$ aggregates of different sizes formed in the electrolyte during discharge (Figure S12 in the SI). We estimate that the discharge capacity that can be achieved with O_2 dissolved in the interior of the CNT carpet alone is ∼20 mAh/g, which is ∼2% of the total discharge capacity (SI). At high rates, these oxygen molecules can be reduced to O_2^--Na^+ species, which could nucleate on the CNT surface to form a coating of solid NaO_2 (2% capacity). Upon continued discharge at high rates, dissolved oxygen molecules in the electrolyte above and beneath the CNT carpet could be reduced to soluble O_2^--Na^+ by the current collector and Na negative electrode, respectively. Given the high discharge rate, the concentration of these soluble O_2^--Na^+ species can quickly build up above and beneath the CNT carpet (Figure S12 in the SI, B1), which can lead to the formation of large $(O_2^-\text{-}Na^+)_n$ aggregates in solution (Figure S12 in the SI, B2). These aggregates are expected to have much lower diffusivity than molecular O_2 and O_2^--Na^+ species and will cluster at the top and bottom of the interfaces of the CNT carpet, where large NaO_2 cubes then grow (Figure S12 in the SI, B3). At low rates, oxygen molecules initially dissolved in the electrolyte are reduced to O_2^--Na^+ species; however, given the low discharge rate, reduced O_2^--Na^+ species form above and beneath the CNT carpet at a slow rate and can diffuse throughout the carpet without quickly aggregating. This results in a more uniform concentration of O_2-Na^+ across the carpet (Figure S12 in the SI, C1) and the formation of smaller $(O_2^-\text{-}Na^+)_n$ aggregates in solution (Figure S12 in the SI, C2) than those formed at high rates. Soluble O_2^--Na^+ species and small $(O_2^-\text{-}Na^+)_n$ aggregates are expected to have greater diffusivity than large $(O_2^-\text{-}Na^+)_n$ aggregates in the electrolyte within the CNT carpet, which results in a more uniform distribution of NaO_2 cubes within the carpet (Figure S12 in the SI, C3). In contrast, during Li_2O_2 formation at similar rates, we observe slower nucleation kinetics to allow the diffusion of reduced oxygen species throughout the whole carpet, thus facilitating more uniform growth.[23]

We support this hypothesis by estimating the difference in thermodynamic barriers to NaO_2 versus Li_2O_2 nucleation from classical nucleation theory, which holds that the thermodynamic barrier for nucleation of a crystal phase ΔG_C depends on its surface energy $\bar{\gamma}$ and the degree of supersaturation of reactants σ[44,45]

$$\Delta G_C \propto \frac{\bar{\gamma}^3}{(-RT \ln \sigma)^2}$$

$\bar{\gamma}$ represents the average surface energy of the crystal, normalized by the area fraction of each exposed facet: $\bar{\gamma} = \sum_i \gamma_i \times A_i$ where γ_i is the surface energy of a particular facet and A_i is its surface area fraction. Using first-principles DFT calculations, Kang et al.[46] have recently estimated a surface energy for the low index {100} terminations of cubic NaO_2 ($P\bar{a}3$) of 11.7 meV/Å^2, resulting in an $\bar{\gamma}$ of 11.7 meV/Å^2. Mo et al.[47] use a similar approximation to DFT as in ref 46 to compute a hexagonal Wulff construction for Li_2O_2 that is dominated by the {0001} and {11$\bar{2}$0} facets with surface energies of 25 and 34 meV/Å^2, respectively, under oxidizing conditions. Assuming a crystal of unit volume with a 64% area fraction composed of the oxygen-rich basal {0001} termination[48] and 36% {11$\bar{2}$0} results in a $\bar{\gamma}$ of 28.2 meV/Å^2, which is ∼2.5 times as high as that of NaO_2. Because ΔG_C is a cubic function of $\bar{\gamma}$, this suggests a nucleation barrier for NaO_2 that is ∼14 times lower than Li_2O_2.

Supersaturation σ is defined as

$$\frac{[a_{M^+}]^y [a_{O_2^{y-}}]}{K_{sp}}$$

where we take $[a_{M^+}]$ and $[a_{O_2^{y-}}]$ to be the solution activities of the alkali metal (M = Na^+ or Li^+) and O_2^{y-} ions, respectively, where y is 1 or 2 for NaO_2 and Li_2O_2, respectively, and K_{sp} is the solubility product of bulk phase NaO_2 or Li_2O_2. To our knowledge, standard K_{sp} values of NaO_2 and Li_2O_2 in DME are not known. For this calculation, we assume that the bulk solid is in equilibrium with its solvated constituent ions such that

$$\mu^o_{Na^+} + \mu^o_{O_2-} - \mu_{NaO_2} = -RT \ln K_{sp}^{NaO_2}$$

$$2\mu^o_{Li^+} + \mu^o_{O_2^{2-}} - \mu_{Li_2O_2} = -RT \ln K_{sp}^{Li_2O_2}$$

where μ^o is the standard state ion formation energy and μ is the chemical potential of the solid. μ for NaO_2 and Li_2O_2 is calculated from their standard values, while $\mu^o_{Na^+}$ and $\mu^o_{Li^+}$ are inferred from regression analysis performed by Gritzner[49]

DOI: 10.1021/acs.jpclett.5b00919
J. Phys. Chem. Lett. 2015, 6, 2636−2643

relating half-wave redox potentials of metal cations to the donor number of the solvent used. Using superoxide and peroxide ion formation energies from redox potentials reported by Sawyer and Gibian,[50] the Li_2O_2 solubility product is $\log_{10} K_{sp}^{Li_2O_2} = -21.7$, while $\log_{10} K_{sp}^{NaO_2} = -18.4$. We approximate activities of soluble ionic species as concentrations. As Li_2O_2 and NaO_2 crystal precursor concentrations in the CNT carpet cannot be directly measured during the ORR, we propose that differences in the solubility of superoxide-related species in 0.1 M $NaClO_4$ versus 0.1 M $LiClO_4$ in DME reflect this difference. From RRDE measurements during the ORR in O_2-saturated 0.1 M $NaClO_4$ in DME, we estimate the fraction of Q_{ORR} charge that is composed of these species to be 60% (Figure 1e), which is in good agreement with the analogous RRDE ring-disk current ratio in 0.1 M NaOTf in DME recently reported by Xia et al.[31] In contrast, this ratio is ∼20% for ORR in Li^+ (Figure 1f). Assuming these solubilities reflect a difference in the actual concentration of soluble O_2^- species during discharge enables us to approximate superoxide supersaturation during NaO_2 than Li_2O_2 growth on the basis of a 10 mM[51] oxygen concentration. This results in supersaturations of 4.6×10^{16} and 1.6×10^{15} for Li_2O_2 and NaO_2 respectively.

Combining this result with the cubic scaling relationship between ΔG_C and $\overline{\gamma}$ yields a nucleation barrier that is ∼12 times smaller for NaO_2 than Li_2O_2 formation and is consistent with the conclusion that NaO_2 nucleation is much faster than Li_2O_2, particularly because the nucleation rate is exponentially dependent on the thermodynamic nucleation barrier. We note that although this analysis does not include quantitative changes to this barrier as a function of discharge overpotential, recent work by Kang et al.[46] suggests that increasing the discharge overpotential decreases nucleation barrier even further from its value at the equilibrium potential. This trend is in agreement with our hypothesis that NaO_2 nucleation is faster at higher rates. We also note that changes to crystal surface energies as a result of solvent molecule adsorption and kinetic barriers to precursor formation such as ion desolvation are not taken in account. Nevertheless, given the ability for such thermodynamic analysis to predict phase selection in several natural/geological mineral systems such as $CaCO_3$[52] and more relevantly, in Na−O_2 batteries,[46] we believe a significant difference in NaO_2 versus Li_2O_2 nucleation barriers is expected and reflects an important first-order difference in the relevant physical parameters dictating relative rates of their bulk phase nucleation. In support of the lower diffusivity of $(O_2^-\text{-}Na^+)_n$ aggregates compared with oxygen, we note that the effective hydrodynamic radius of O_2 in DME is 0.12 nm,[51] while the size of the critical nucleus of NaO_2 at 1 atm has been calculated at ∼1 nm for discharge potentials <2.0 V versus Na^+/Na.[46] Assuming $(O_2^-\text{-}Na^+)_n$ aggregates nucleated in solution are of roughly the size of critical NaO_2 radii and that their diffusivity as well as that of O_2 follows the Stokes−Einstein relation (where diffusivity is inversely proportional to hydrodynamic radius), the diffusivity of the aggregates will be expected to be ∼10 times less than that of molecular O_2.

In summary, the sole discharge product after Na−O_2 cell discharge is sodium superoxide (NaO_2), as indicated by XRD and Raman spectroscopy. NaO_2 can convert to $Na_2O_2{\cdot}2H_2O$ upon exposure to ambient atmosphere, but $Na_2O_2{\cdot}2H_2O$ cannot be formed in Na−O_2 cells, even when 6000 ppm of H_2O is added to the electrolyte. Discharge at low rates results in micron-scale and nanometer-scale NaO_2 cubes on the top and bottom of CNT carpets and along the CNTs in the interior of the carpet, while at high rates, micron-scale NaO_2 cubes form only on the top and bottom surfaces of CNT carpets and no nanoscale NaO_2 particles are detected along CNT sidewalls in the interior of the carpets. We explain this difference on the basis of high local supersaturation and thus fast nucleation of $(O_2^-\text{-}Na^+)_n$ aggregates with low mobility at the oxygenated top and bottom interfaces of the CNT carpet at high rates but lower supersaturation, slower nucleation of $(O_2^-\text{-}Na^+)_n$ aggregates, greater diffusion throughout the CNT carpet, and thus more uniform growth, at lower rates. We justify the importance of the competition between NaO_2 crystal nucleation kinetics and precursor diffusion by showing that the estimated thermodynamic barrier for NaO_2 nucleation is 12 times lower than that for Li_2O_2, implying faster NaO_2 growth kinetics. This is consistent with the rate dependence of the spatial distribution of NaO_2 previously outlined and more uniform discharge product formation for Li_2O_2 growth at both low and high discharge rates. The insights obtained from integrating electrochemical, structural, chemical, and kinetic components involved in Na−O_2 battery discharge could enable new strategies for maximizing energy density of practical Na−O_2 electrodes.

EXPERIMENTAL METHODS

Cyclic Voltammetry Measurements. Three-electrode cells consisted of a 5 mm diameter GC disk as the working electrode (5 mm diameter), an Au ring electrode (6.5 mm inner diameter, 7.5 mm outer diameter), and a sodium or lithium foil counter and reference electrode. RRDE experiments were performed in a water-free argon glovebox (H_2O < 0.1 ppm, O_2 < 1%). 0.1 M $LiClO_4$ in DME was purchased from BASF, USA and used as received, while 0.1 M $NaClO_4$ in DME was prepared. $NaClO_4$ salt was purchased from Sigma-Aldrich and vacuum-dried at 150 °C for 24 h prior to electrolyte mixing. RRDE measurements were performed in O_2-saturated electrolyte by sweeping the disk between 1.8 and 4.0 V versus Na^+/Na, while the ring is held at 3.0 V versus Na^+/Na to oxidize soluble O_2^- species convected to it from the disk under rotation up to 1600 rpm. In the analogous Li−O_2 case, the disk was swept between 2.0 and 4.5 V versus Li^+/Li, while the ring is held at 3.5 V versus Li^+/Li. We assume the ring oxidation charge reflects the detection of solution-based O_2^- species produced during ORR and estimate the fraction of Q_{ORR} charge that is composed of these species by normalizing it to the theoretical collection efficiency, η, of the RRDE geometry: $Q_{ring}/\eta Q_{ORR}$, where in our case, η is 23.5%. η was calibrated using the reversible O_2/O_2^- couple in dimethyl sulfoxide; however, the collection efficiency using the well-known ferrocene/ferrocenium (Fc/Fc^+) couple yielded a similar value of 25.8%. The other component of Q_{ORR} thus reflects surface-bound or insoluble species, represented by Q_{OER}/Q_{ORR}.

Cell Assembly and Electrochemical Measurements. The fabricated Na−O_2 cells consisted of a sodium metal anode and freestanding vertically aligned few-walled CNT carpets (detailed preparation of the nanotubes has been previously reported[39,50]) as the O_2 electrode (∼1 × 1 cm). The electrodes were vacuum-dried at 100 °C for 8 h and transferred to a glovebox (H_2O < 0.1 ppm, O_2 < 0.1 ppm, Mbraun, USA) without exposure to the ambient environment. Carbon loading of ∼1 mg/cm^2 was used. Ethylene glycol dimethyl ether, ($C_4H_{10}O_2$, DME), (anhydrous, 99.5% Sigma-Aldrich) was used as the electrolyte solvent and sodium perchlorate ($NaClO_4$, 98%, Sigma-Aldrich) as the conducting salt. DME and sodium

DOI: 10.1021/acs.jpclett.5b00919
J. Phys. Chem. Lett. 2015, 6, 2636−2643

perchlorate were dried over molecular sieves (3 Å) for 1 week and under vacuum at 150 °C for 24 h, respectively. The electrolyte solution of 0.1 M $NaClO_4$ in DME was prepared in a glovebox with a final water content of <10 ppm, determined by C20 Karl Fisher coulometer (Mettler Toledo). Cells were assembled with sodium metal (Sigma-Aldrich, 15 mm in diameter) and two Celgard C480 separators (Celgard, USA, 18 mm diameter) were soaked in 120 μL of electrolyte. A stainless-steel mesh was used as the current collector. Following assembly, cells were transferred to another connected argon glovebox (Mbraun, USA, H_2O < 1 ppm, O_2 < 1%) without exposure to air and pressurized to 25 psi (gage) with dry O_2 (99.994% pure O_2, Airgas, H_2O < 2 ppm) to ensure adequate O_2 inside the cells. Electrochemical tests were conducted using a Biologic VMP3. Galvanostatic discharge tests were performed by first resting at open circuit (~2.2 to 2.5 V vs Na^+/Na) for 3 h prior to applying current.

X-ray Diffraction Characterization. XRD patterns on electrochemically discharged electrodes were collected using a Rigaku Smartlab (Rigaku, Salem, NH) in the surface-sensitive parallel beam configuration. The CNT electrodes were extracted from the Na−O_2 cell immediately after discharge in an argon-filled glovebox and sealed in an airtight XRD sample holder (Anton Paar, Graz, Austria), featuring an X-ray transparent plastic dome, sealed with a rubber O-ring, in order to minimize exposure to atmospheric contaminants before and during XRD measurements.

Raman Spectroscopy Measurements. Raman spectroscopy was conducted on the discharged electrodes in a LabRAM HR800 microscope (Horiba Jobin Yvon) using an external 20 mW He:Ne 523 nm laser (Horiba, Jobin Yvon), focused with a 50× long working distance objective. A silicon wafer was used for calibration.

SEM Characterization. SEM images were taken using a Zeiss Supra55VP and Ultra55 (Carl Zeiss AG, Germany). Images were taken with an in-lens detector at 5 kV operating voltage. Samples were sealed and stored in argon before being rapidly moved into the SEM chamber to minimize air exposure.

TEM Characterization. High-voltage TEM studies were performed at 200 kV on a JEOL 2010F microscope. Energy-dispersive spectroscopy (EDS) data were collected and analyzed using Inca (Oxford Instruments) software. Low-voltage TEM studies were performed at 40 kV on a FEI Tecnai (G2 Spirit TWIN) multipurpose TEM.

■ ASSOCIATED CONTENT

Ⓢ Supporting Information

Additional characterization data. The Supporting Information is available free of charge on the ACS Publications website at DOI: 10.1021/acs.jpclett.5b00919.

■ AUTHOR INFORMATION

Corresponding Authors

*E-mail: nagore@mit.edu (N.O.-V.).
*E-mail: cthomp@mit.edu (C.V.T.)
*E-mail: shaohorn@mit.edu (Y.S.-H.)

Author Contributions

#N.O.-V., T.P.B., and D.G.K. contributed equally to this work

Notes

The authors declare no competing financial interest.

■ ACKNOWLEDGMENTS

This work was supported by a Marie Curie International Outgoing Fellowship within the EU Seventh Framework Programme for Research and Technological Development (2007-2013) for N.O.-V. and in part by the MRSEC Program of the National Science Foundation under award number DMR-0819762, the Robert Bosch Company with a Bosch Energy Research Network Grant, and the CERC−CVC US China Clean Energy Research Center-Clean Vehicles Consortium of the Department of Energy (under award number DE-PI0000012). T.P.B. was supported in part by the Center for Electrochemical Energy Storage of the Skolkovo Institute of Science and Technology. SEM imaging was performed at the Center for Nanoscale Systems (CNS), a member of the National Nanotechnology Infrastructure Network (NNIN), which is supported by the National Science Foundation under NSF award no. ECS-0335765. CNS is part of Harvard University. We thank Wenhao Sun for useful discussions.

■ REFERENCES

(1) Lu, Y.-C.; Gallant, B. M.; Kwabi, D. G.; Harding, J. R.; Mitchell, R. R.; Whittingham, M. S.; Shao-Horn, Y. Lithium−oxygen Batteries: Bridging Mechanistic Understanding and Battery Performance. *Energy Environ. Sci.* **2013**, *6*, 750.

(2) Kwabi, D. G.; Ortiz-Vitoriano, N.; Freunberger, S. A.; Chen, Y.; Imanishi, N.; Bruce, P. G.; Shao-Horn, Y. Materials Challenges in Rechargeable Lithium-Air Batteries. *MRS Bull.* **2014**, *39*, 443−452.

(3) Lee, J.-S.; Tai Kim, S.; Cao, R.; Choi, N.-S.; Liu, M.; Lee, K. T.; Cho, J. Metal-Air Batteries with High Energy Density: Li-Air versus Zn-Air. *Adv. Energy Mater.* **2011**, *1*, 34−50.

(4) Bruce, P. G.; Freunberger, S. A.; Hardwick, L. J.; Tarascon, J.-M. Li-O_2 and Li-S Batteries with High Energy Storage. *Nat. Mater.* **2012**, *11*, 19−29.

(5) Black, R.; Adams, B.; Nazar, L. F. Non-Aqueous and Hybrid Li-O_2 Batteries. *Adv. Energy Mater.* **2012**, *2*, 801−815.

(6) Abraham, K. M. A Polymer Electrolyte-Based Rechargeable Lithium/Oxygen Battery. *J. Electrochem. Soc.* **1996**, *143*, 1.

(7) Freunberger, S. A.; Chen, Y.; Drewett, N. E.; Hardwick, L. J.; Bardé, F.; Bruce, P. G. The Lithium-Oxygen Battery with Ether-Based Electrolytes. *Angew. Chem., Int. Ed.* **2011**, *50*, 8609−8613.

(8) McCloskey, B. D.; Bethune, D. S.; Shelby, R. M.; Girishkumar, G.; Luntz, A. C. Solvents' Critical Role in Nonaqueous Lithium−Oxygen Battery Electrochemistry. *J. Phys. Chem. Lett.* **2011**, *2*, 1161−1166.

(9) Kwabi, D. G.; Batcho, T. P.; Amanchukwu, C. V.; Ortiz-Vitoriano, N.; Hammond, P.; Thompson, C. V.; Shao-Horn, Y. Chemical Instability of Dimethyl Sulfoxide in Lithium−Air Batteries. *J. Phys. Chem. Lett.* **2014**, *5*, 2850−2856.

(10) Gallant, B. M.; Mitchell, R. R.; Kwabi, D. G.; Zhou, J.; Zuin, L.; Thompson, C. V.; Shao-Horn, Y. Chemical and Morphological Changes of Li−O 2 Battery Electrodes upon Cycling. *J. Phys. Chem. C* **2012**, *116*, 20800−20805.

(11) Ottakam Thotiyl, M. M.; Freunberger, S. A.; Peng, Z.; Chen, Y.; Liu, Z.; Bruce, P. G. A Stable Cathode for the Aprotic Li−O_2 Battery. *Nat. Mater.* **2013**, *12*, 1050−1056.

(12) Hartmann, P.; Bender, C. L.; Vračar, M.; Dürr, A. K.; Garsuch, A.; Janek, J.; Adelhelm, P. A Rechargeable Room-Temperature Sodium Superoxide (NaO_2) Battery. *Nat. Mater.* **2013**, *12*, 228−232.

(13) Hartmann, P.; Bender, C. L.; Sann, J.; Dürr, A. K.; Jansen, M.; Janek, J.; Adelhelm, P. A Comprehensive Study on the Cell Chemistry of the Sodium Superoxide (NaO_2) Battery. *Phys. Chem. Chem. Phys.* **2013**, *15*, 11661−11672.

(14) Bender, C. L.; Hartmann, P.; Vračar, M.; Adelhelm, P.; Janek, J. On the Thermodynamics, the Role of the Carbon Cathode, and the Cycle Life of the Sodium Superoxide (NaO_2) Battery. *Adv. Energy Mater.* **2014**, *4*.

DOI: 10.1021/acs.jpclett.5b00919
J. Phys. Chem. Lett. 2015, 6, 2636−2643

(15) McCloskey, B. D.; Garcia, J. M.; Luntz, A. C. Chemical and Electrochemical Differences in Non-Aqueous Li-O_2 and Na-O_2 Batteries. *J. Phys. Chem. Lett.* **2014**, *5* (7), 1230−1235.
(16) Liu, W.; Sun, Q.; Yang, Y.; Xie, J.-Y.; Fu, Z.-W. An Enhanced Electrochemical Performance of a Sodium-Air Battery with Graphene Nanosheets as Air Electrode Catalysts. *Chem. Commun.* **2013**, *49*, 1951−1953.
(17) Sun, Q.; Yang, Y.; Fu, Z.-W. Electrochemical Properties of Room Temperature Sodium−air Batteries with Non-Aqueous Electrolyte. *Electrochem. Commun.* **2012**, *16*, 22−25.
(18) Kim, J.; Lim, H.-D.; Gwon, H.; Kang, K. Sodium-Oxygen Batteries with Alkyl-Carbonate and Ether Based Electrolytes. *Phys. Chem. Chem. Phys.* **2013**, *15*, 3623−3629.
(19) Jian, Z.; Chen, Y.; Li, F.; Zhang, T.; Liu, C.; Zhou, H. High Capacity Na−O_2 Batteries with Carbon Nanotube Paper as Binder-Free Air Cathode. *J. Power Sources* **2014**, *251*, 466−469.
(20) Yadegari, H.; Li, Y.; Norouzi Banis, M.; Li, X.; Wang, B.; Sun, Q.; Li, R.; Sham, T.-K.; Cui, X.; Sun, X. On Rechargeability and Reaction Kinetics of Sodium-Air Batteries. *Energy Environ. Sci.* **2014**, *7*, 3747−3757.
(21) Bender, C. L.; Bartuli, W.; Schwab, M. G.; Adelhelm, P.; Janek, J. Toward Better Sodium-Oxygen Batteries: A Study on the Performance of Engineered Oxygen Electrodes Based on Carbon Nanotubes. *Energy Technol.* **2015**, *3*, 242−248.
(22) Sun, Q.; Yadegari, H.; Banis, M. N.; Liu, J.; Xiao, B.; Wang, B.; Lawes, S.; Li, X.; Li, R.; Sun, X. Self-Stacked Nitrogen-Doped Carbon Nanotubes as Long-Life Air Electrode for Sodium-Air Batteries: Elucidating the Evolution of Discharge Product Morphology. *Nano Energy* **2015**, *12*, 698−708.
(23) Gallant, B. M.; Kwabi, D. G.; Mitchell, R. R.; Zhou, J.; Thompson, C. V.; Shao-Horn, Y. Influence of Li_2O_2 Morphology on Oxygen Reduction and Evolution Kinetics in Li−O_2 Batteries. *Energy Environ. Sci.* **2013**, *6*, 2518−2528.
(24) Mitchell, R. R.; Gallant, B. M.; Thompson, C. V.; Shao-Horn, Y. All-Carbon-Nanofiber Electrodes for High-Energy Rechargeable Li−O_2 Batteries. *Energy Environ. Sci.* **2011**, *4*, 2952−2958.
(25) Lu, Y.-C.; Shao-Horn, Y. Probing the Reaction Kinetics of the Charge Reactions of Nonaqueous Li−O_2 Batteries. *J. Phys. Chem. Lett.* **2013**, *4*, 93−99.
(26) Viswanathan, V.; Nørskov, J. K.; Speidel, A.; Scheffler, R.; Gowda, S.; Luntz, A. C. Li−O_2 Kinetic Overpotentials: Tafel Plots from Experiment and First-Principles Theory. *J. Phys. Chem. Lett.* **2013**, *4*, 556−560.
(27) Safari, M.; Adams, B. D.; Nazar, L. F. Kinetics of Oxygen Reduction in Aprotic Li-O_2 Cells: A Model-Based Study. *J. Phys. Chem. Lett.* **2014**, 140922111651002.
(28) Bai, P.; Bazant, M. Z. Charge Transfer Kinetics at the Solid-Solid Interface in Porous Electrodes. *Nat. Commun.* **2014**, *5*, 3585.
(29) Ganapathy, S.; Adams, B. D.; Stenou, G.; Anastasaki, M. S.; Goubitz, K.; Miao, X.-F.; Nazar, L. F.; Wagemaker, M. Nature of Li_2O_2 Oxidation in a Li-O_2 Battery Revealed by Operando X-Ray Diffraction. *J. Am. Chem. Soc.* **2014**, *136*, 16335−16344.
(30) Bösch, H. M.; Känzig, W.; Steigmeier, E. F. Molekül- Und Gitterschwingungen Im Natriumhyperoxid. *Phys. Kondens. Mater.* **1973**, *16*, 107−112.
(31) Xia, C.; Black, R.; Fernandes, R.; Adams, B.; Nazar, L. F. The Critical Role of Phase-Transfer Catalysis in Aprotic Sodium Oxygen Batteries. *Nat. Chem.* **2015**, *7*, 496−501.
(32) Lee, B. J.; Seo, D.-H.; Lim, H.-D.; Park, I.; Park, K.-Y.; Kim, J.; Kang, K. First-Principles Study of the Reaction Mechanism in Sodium-Oxygen Batteries. *Chem. Mater.* **2014**, *26*, 1048−1055.
(33) Schoonen, M. A. A. Mechanisms of Sedimentary Pyrite Formation. *Geol. Soc. Am.* **2004**, *379*, 117−134.
(34) Zhuravlev, Y. N.; Kravchenko, N. G.; Obolonskaya, O. S. The Electronic Structure of Alkali Metal Oxides. *Russ. J. Phys. Chem. B* **2010**, *4*, 20−28.
(35) Bertel, E.; Memmel, N.; Jacob, W.; Dose, V.; Netzer, F.; Rosina, G.; Rangelov, G.; Astl, G.; Rösch, N.; Knappe, P.; et al. Alkali-Metal Oxides. II. Unoccupied and Excited States. *Phys. Rev. B* **1989**, *39*, 6087−6095.
(36) Arcelus, O.; Li, C.; Rojo, T.; Carrasco, J. Electronic Structure of Sodium Superoxide Bulk, (100) Surface, and Clusters Using Hybrid Density Functional: Relevance for Na−O_2 Batteries. *J. Phys. Chem. Lett.* **2015**, 2027−2031.
(37) Yang, S.; Siegel, D. J. Intrinsic Conductivity in Sodium−Air Battery Discharge Phases: Sodium Superoxide vs Sodium Peroxide. *Chem. Mater.* **2015**, *27*, 3852−3860.
(38) Cölfen, H.; Mann, S. Higher-Order Organization by Mesoscale Self-Assembly and Transformation of Hybrid Nanostructures. *Angew. Chem., Int. Ed* **2003**, *42*, 2350−2365.
(39) Johnson, L.; Li, C.; Liu, Z.; Chen, Y.; Freunberger, S. A.; Tarascon, J.-M.; Ashok, P. C.; Praveen, B. B.; Dholakia, K.; Bruce, P. G. The Role of LiO_2 Solubility in O_2 Reduction in Aprotic Solvents and Its Consequences for Li−O_2 Batteries. *Nat. Chem.* **2014**, *6*, 1091−1099.
(40) Aetukuri, N. B.; McCloskey, B. D.; García, J. M.; Krupp, L. E.; Viswanathan, V.; Luntz, A. C. Solvating Additives Drive Solution-Mediated Electrochemistry and Enhance Toroid Growth in Non-Aqueous Li-O_2Batteries. *Nat. Chem.* **2015**, *7*, 50−56.
(41) Lu, Y.-C.; Kwabi, D. G.; Yao, K. P. C.; Harding, J. R.; Zhou, J.; Zuin, L.; Shao-Horn, Y. The Discharge Rate Capability of Rechargeable Li−O_2 Batteries. *Energy Environ. Sci.* **2011**, *4*, 2999−3007.
(42) Hartmann, P.; Grübl, D.; Sommer, H.; Janek, J.; Bessler, W. G.; Adelhelm, P. Pressure Dynamics in Metal-Oxygen (Metal-Air) Batteries: A Case Study on Sodium Superoxide (NaO_2) Cells. *J. Phys. Chem. C* **2014**, *118*, 1461−1471.
(43) Mitchell, R. R.; Gallant, B. M.; Shao-Horn, Y.; Thompson, C. V. Mechanisms of Morphological Evolution of Li_2O_2 Particles during Electrochemical Growth. *J. Phys. Chem. Lett.* **2013**, *4*, 1060−1064.
(44) Stranski, I.; Totomanow, Z. Rate of Formation of (Crystal) Nuclei and the Ostwald Step Rule. *Phys. Chem.* **1933**, *163*, 399−408.
(45) Baumgartner, J.; Dey, A.; Bomans, P. H. H.; Le Coadou, C.; Fratzl, P.; Sommerdijk, N. A. J. M.; Faivre, D. Nucleation and Growth of Magnetite from Solution. *Nat. Mater.* **2013**, *12*, 310−314.
(46) Kang, S.; Mo, Y.; Ong, S. P.; Ceder, G. Nanoscale Stabilization of Sodium Oxides: Implications for Na-O_2 Batteries. *Nano Lett.* **2014**, *14*, 1016−1020.
(47) Mo, Y.; Ong, S. P.; Ceder, G. First-Principles Study of the Oxygen Evolution Reaction of Lithium Peroxide in the Lithium-Air Battery. *Phys. Rev. B* **2011**, *84*, 205446.
(48) Radin, M. D.; Rodriguez, J. F.; Tian, F.; Siegel, D. J. Lithium Peroxide Surfaces Are Metallic, While Lithium Oxide Surfaces Are Not. *J. Am. Chem. Soc.* **2012**, *134*, 1093−1103.
(49) Gritzner, G. Solvent Effects on Half-Wave Potentials. *J. Phys. Chem.* **1986**, *90*, 5478−5485.
(50) Sawyer, D. T.; Gibian, M. J. The Chemistry of Superoxide Ion. *Tetrahedron* **1979**, *35*, 1471−1481.
(51) Read, J.; Mutolo, K.; Ervin, M.; Behl, W.; Wolfenstine, J.; Driedger, A.; Foster, D. Oxygen Transport Properties of Organic Electrolytes and Performance of Lithium/Oxygen Battery. *J. Electrochem. Soc.* **2003**, *150*, A1351−A1356.
(52) Sun, W.; Jayaraman, S.; Chen, W.; Persson, K. A.; Ceder, G. Nucleation of Metastable Aragonite $CaCO_3$ in Seawater. *Proc. Natl. Acad. Sci. U. S. A.* **2015**, *112*, 3199−3204.

DOI: 10.1021/acs.jpclett.5b00919
J. Phys. Chem. Lett. 2015, 6, 2636−2643